Design and Analysis of Lithium–Niobate–Based High Electromechanical Coupling RF-MEMS Resonators for Wideband Filtering

Article *in* IEEE Transactions on Microwave Theory and Techniques · January 2013

DOI: 10.1109/TMTT.2012.2228671

Design and Analysis of Lithium–Niobate-Based High Electromechanical Coupling RF-MEMS Resonators for Wideband Filtering

Songbin Gong, *Associate Member, IEEE*, and Gianluca Piazza, *Member, IEEE*

***Abstract*—This paper reports on a new type of microresonators enabled by micromachining of ion sliced X-cut $LiNbO_3$ thin films. In operation, the device is excited into lateral vibrations, thus allowing the center frequency to be determined by the lithographically defined dimensions of the excitation electrodes. The demonstrated device has a high electromechanical coupling (k_t^2) of 11.5%—the highest attained for laterally vibrating microelectromechanical systems resonators. Device orientation was also varied to investigate its impact on k_t^2 and experimental data have shown good agreement with theoretical predictions. Several key performance parameters, including the quality factor (Q), the static capacitance, C_0, the temperature coefficient of frequency (TCF), and the power handling, are also characterized and the related experimental data are presented. The devices demonstrate Q's up to 1800. The measured TCFs range from -55 to -69 ppm/K and can be considered sufficiently low for wideband RF filtering. The high electromechanical coupling and the high Q of this new class of devices show promise for the implementation of multifrequency wideband multiplexers and filter banks for reconfigurable RF front-ends.**

***Index Terms*—High electromechanical coupling, lamb wave, lithium–niobate (LN), piezoelectric resonators, wideband filters.**

I. Introduction

IN RESPONSE to customers' increasing need for more types of services in handheld mobile units, modern wireless systems have evolved toward high integration of components with multiple functionalities. To maintain a small form factor while accommodating more functionalities, single-chip and high-performance multiplexers are required for selecting between various operational bands. All existing duplexers resort to acoustic resonators for their implementation. To attain high performance and wide bandwidth, high electromechanical coupling, and quality factor, Q, are simultaneously needed for the resonators that are used in such duplexers. As seen in Fig. 1, the electromechanical coupling coefficient (k_t^2) is directly related to the fractional bandwidth (FBW) of the filters for different topologies, and along with the quality factor determines the insertion loss.

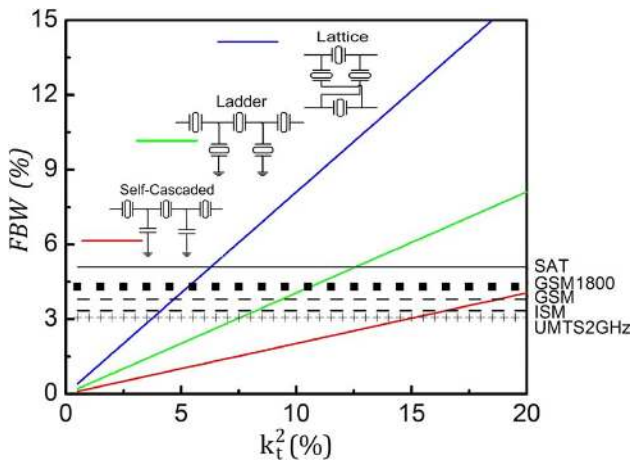

Fig. 1. Relationship between electromechanical coupling and filter FBW for three types of filter configurations.

In the last decade, piezoelectric thin film resonators, such as thin film bulk acoustic-wave resonators (FBARs) [1], [2] and solid mounted resonators (SMRs) [3], have successfully demonstrated the capability of forming duplexers, owning to the high $d_{33}(k_t^2 = 7\%)$ and high Q of the AlN films. However, it is challenging to implement monolithic multiband solutions with such devices since their center frequencies are set by the film thickness. Width-extensional mode resonators, which have lithographically defined resonances and can cover multiple frequencies on the same wafer, have also been demonstrated using AlN thin films [4]. These device are limited to narrowband or oscillator applications due to the moderate $d_{31}(k_t^2 = 2\%)$ of AlN. Other materials, including lead zirconate titanate (PZT), quartz and barium strontium titanate (BST), and device actuation (Si electrostatic) have also been explored for laterally vibrating (width extensional) resonators (Table I). Nonetheless, none of them can simultaneously meet the high k_t^2 and high Q requirements for next-generation reconfigurable and multifrequency wideband filtering. Lithium–niobate (LN)-based microresonators are considered to be a promising solution for wideband and high Q operation due to the high k_t^2 and very low phonon–phonon dissipation intrinsic to LN. In particular, its high k_t^2 enables it to implement tuning functionalities not presently possible even with AlN FBARs [5]. Moreover, the recently demonstrated LN high-overtone bulk acoustic resonators

Manuscript received July 11, 2012; revised October 20, 2012; accepted October 23, 2012. Date of publication December 13, 2012; date of current version January 17, 2013. This work was supported by the Defense Advanced Research Projects Agency (DARPA) and the Northrop Grumman Corporation under the N/MEMS S&T Program. This paper is an expanded paper from the IEEE MTT-S International Microwave Symposium, Montreal, QC, Canada, June 17–22, 2012.

The authors are with the Department of Electrical and Computer Engineering, Carnegie Mellon University, Pittsburgh, PA 15213 USA (e-mail: songbing@andrew.cmu.edu; piazza@ece.cmu.edu).

Color versions of one or more of the figures in this paper are available online at http://ieeexplore.ieee.org.

Digital Object Identifier 10.1109/TMTT.2012.2228671

TABLE I
k_t^2 AND Q PERFORMANCE OF THE STATE-OF-THE-ART

Device	k_t^2	Q	Ref
AlN-FBAR	7%	2500@2 GHz	[1]
PZT-FBAR	12%	58@1 GHz	[2]
BST-FBAR	7.07%	230@2 GHz	[8]
AlN-CMR	2%	3000@0.5 GHz	[9][4]
LN/LT SAW	20%	1000@ 2 GHz	[10]
LN-FBAR	35%	100@ 1 GHz	[11]
Si-Electrostatic	<0.1%	>10000@ 60 MHz	[12]
This Work	up to 11.5%	up to 1800@ 0.5 GHz	[13]

(HBARs) with a $f \cdot Q$ product of 5×10^{13} have experimentally verified low intrinsic acoustic loss of the LN material [6]. Surface acoustic wave (SAW) devices using LN are already the industry standard for RF filters below 2 GHz. Nevertheless, the low phase velocity (3500 m/s) and lack of defined acoustic boundaries in SAW configurations limit the scaling of these devices, their Q, and their extension to multiband operations at higher frequencies (>2 GHz).

This work focuses on the development of a new class of devices using ion sliced LN thin films. The device introduced herein is similar to the AlN-based contour mode resonators previously demonstrated for narrowband applications [7]. In operation, the device is excited into lateral vibrations. The center frequency is determined by the lateral dimensions (pitch) of the metal electrodes used for exciting the resonator into motion. This configuration enables the lithographical definition of multiple frequencies on a single chip. In addition, the full suspension of the resonant structure efficiently traps energy and enhances Q. More importantly, the high phase velocity (7000 m/s) of the selected $S0$ lamb wave mode makes possible envisioning higher frequencies of operation (3–5 GHz) using the same lithography resolution of SAW devices. The fabricated prototype devices, with a center frequency of 530 MHz, have demonstrated a k_t^2 of 11.5%, the highest among any laterally vibrating microelectromechanical systems (MEMS) resonators to date. This type of device is considered to be an excellent fit for a broad range of applications including wideband multiplexers and reconfigurable RF-frond ends.

This paper is organized as follows. In Section II, theoretical calculations of electromechanical coupling are carried out for the $S0$ mode acoustic wave in LN thin film to identify X-cut as the optimum LN for wideband operations. Detailed design and modeling techniques for this type of resonators are presented in Section III. The challenges of micromachining LN are discussed and the adopted fabrication process is presented in Section IV. In Section V, the performance of these devices are experimentally investigated and compared to the theoretical analysis. Several key performance parameters, including k_t^2, Q, C_0, temperature coefficient of frequency (TCF), and power handling are reported and discussed. Section VI concludes this paper by summarizing the contributions of this paper and setting some directions for future work.

II. $S0$-MODE LAMB WAVE IN LN THIN FILM

LN has been used for SAW devices in the past to build wideband filters. Despite the low cost and simplicity of SAW device designs, limitations exist due to the nature of SAW modes. Due to the recent advancement of thin film transfer technology, a number of materials now can be obtained in thin film form with crystal quality close to the bulk counterparts on either Si or the same material substrates [14]–[16]. This opens up the possibility of building $S0$-mode bulk acoustic wave devices that have been demonstrated with AlN [4], ZnO [17], and PZT [18], but yet unexplored with materials such as LN. The high piezoelectric coefficients and anisotropy of LN material have attracted considerable attention from RF and MEMS communities. The piezoelectric coefficient is directly related to the electromechanical coupling by

$$K_{ij} = \frac{e_{ij}}{\sqrt{\varepsilon_{ij} C_{ij}}} \tag{1}$$

where the indices i and j refer to the direction along which the electric field is applied and the corresponding direction of motion, respectively; e_{ij} is the corresponding piezoelectric coefficient; C_{ij} is the corresponding compliance value; and ε_{ij} is the relative permittivity associated with the particular mode of vibration. The K_{ij}^2 of LN devices vibrating in the $S0$ mode can be readily estimated by comparing the phase velocities of the same acoustic mode in a thin LN plate with and without perfect metallized boundary condition on the top surface. This technique is described in more details in [19]. Finite-element method (FEM) analysis was used to model the dependence of k_t^2 on the in-plane orientation for each unrotated crystal cut. The K^2, which directly related to $k_t^2 (k_t^2 = K^2/(1+K^2))$, can be calculated as

$$K^2 = \frac{v_m^2 - v_0^2}{v_0^2} \tag{2}$$

where v_m is the phase velocity for the $S0$ mode with a metallized surface and v_0 is the phase velocity for the $S0$-mode lamb wave with free boundary conditions. The simulation (Fig. 2) has shown that the K^2 and phase velocity changes as the orientation varies from 0° to 180° within each cut planes. The X-cut LN with a 30° orientation has the highest K^2 (35%) among all cuts and orientations. The phase velocity of $S0$-mode lamb waves is between 6400–7200 m/s, with X-cut having the highest average phase velocity. This analysis indicates that the X-cut is the optimum cut LN for enabling high electromechanical coupling (k_t^2) microresonators.

III. DEVICE DESIGN AND MODELING

As shown in Fig. 3(a), the device consists of metal inter-digital fingers on top of a mechanically suspended LN thin film. The electric field induced by the inter-digitated transducers (IDTs) that are alternatively connected to ground and signal [see Fig. 3(b)] excites lateral expansion and compression in adjacent fingers (mode known as $S0$ lamb wave). The mechanical resonance of such operation is a function of the lateral dimension of the excitation electrode and can be formulated as

$$f_0 = \frac{v}{2W_p} \tag{3}$$

where v is the acoustic phase velocity and W_p is the electrode pitch. Similarly to other acoustic resonators, it can be readily modeled using the modified Butterworth–Van Dyke (MBVD) model shown in Fig. 3(c), in which C_m (motional capacitance),

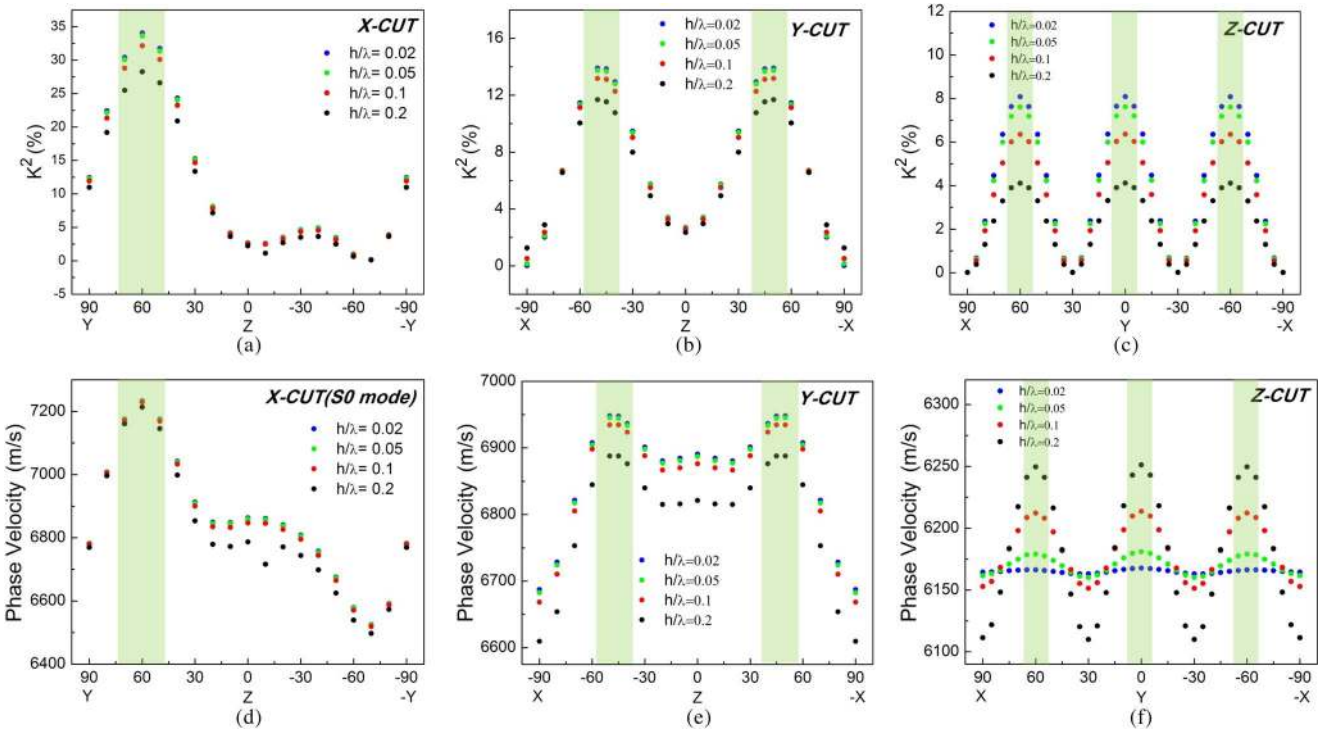

Fig. 2. Simulated K^2 and phase velocity for various cut of LN. h is the thickness of LN thin film, and λ is the acoustic wavelength. (a) K^2 of $S0$ mode for X-cut. (b) K^2 of $S0$ mode for Y-cut. (c) K^2 of $S0$ mode for Z-cut. (d) Phase velocity of $S0$ mode for X-cut. (e) Phase velocity of $S0$ mode for Y-cut. (f) Phase velocity of $S0$ mode for Z-cut.

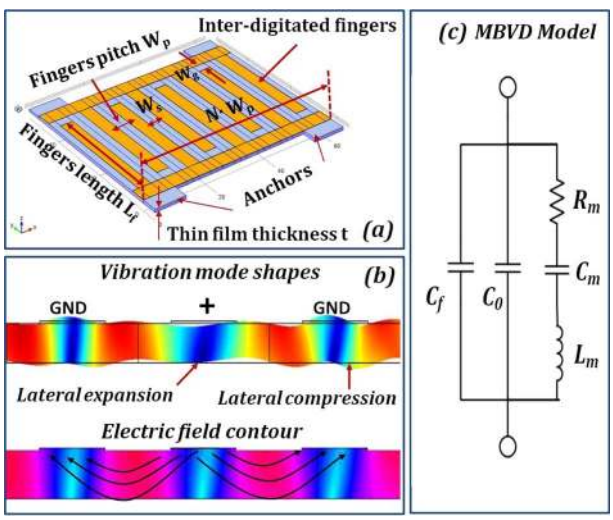

Fig. 3. (a) 3-D mocked up view of a corner anchored LN microresonator. (b) Displacement mode shape and electric field contour obtained from COMSOL FEM analysis. (c) MBVD model for the resonator.

L_m (motional inductance), and R_m (motional resistance) are used to represent the components induced by the mechanical motion of the device. R_m is inversely related to $k_t^2 \cdot Q$ and the static capacitance in between the IDT, C_0. These equivalent parameters can be expressed as [4]

$$R_m = \frac{\pi^2}{8}\frac{1}{\omega_s C_0}\frac{1}{k_t^2 Q} \tag{4}$$

$$L_m = \frac{\pi^2}{8}\frac{1}{\omega_s^2 C_0}\frac{1}{k_t^2} \tag{5}$$

$$C_m = \frac{8}{\pi^2} C_0 k_t^2. \tag{6}$$

C_0 is a function of finger pitch (W_p), length (L_f), and spacing (W_s). C_0 can be derived with well-known techniques for IDT capacitors and the FEM method [20]. The detailed analysis of C_0 and its impact on device performance are presented in Section V-B. C_f is the parasitic feed-through capacitance whose origin will be discussed in Section V-B as well. Naturally, a high $k_t^2 \cdot Q$, the figure of merit (FOM) for piezoelectric microresonators, is desired to enable low loss and low impedance for interfacing with RF electronics. The ultimate k_t^2 of the device is determined collectively by the piezoelectric material and the electrode configuration.

Although the simulation results shown in Fig. 2(a) give insights on the dependence of the electromechanical coupling on orientations and cuts, they only present theoretical limits and do not predict the actual electromechanical coupling achievable by a particular resonator geometry. 2-D COMSOL simulations are thus carried out to fully investigate the k_t^2 for various electrode configurations. The simulation is done by first acquiring the rotated stiffness and piezoelectric coupling matrix for each cut and orientation. The rotated stiffness, coupling and permittivity matrices for any orientations and cuts can be readily found using the transformation matrix and bond matrix M [21]

$$\widetilde{cE} = M \cdot cE \cdot M^t \tag{7}$$

$$\tilde{e} = a \cdot e \cdot M^t \tag{8}$$

$$\tilde{\varepsilon} = a \cdot \varepsilon \cdot a^t \tag{9}$$

TABLE II
MATERIAL CONSTANTS USED IN THE SIMULATIONS

	Symbol	Lithium Niobate [22]	Temperature Coeff (ppm/K) [23]
Elastic Constants ($10^{11} N/m^2$) and their Temp Coefficients (ppm/K)	c_{11}	19.839	-174
	c_{12}	5.472	-252
	c_{13}	6.512	-159
	c_{14}	0.788	-214
	c_{33}	22.790	-153
	c_{44}	0.5965	-203
	c_{66}	0.75	-143
Piezoelectric Constants (C/m^2)	e_{15}	3.69	
	e_{22}	2.42	
	e_{31}	0.30	
	e_{33}	1.77	
Dielectric Constants	ε_{11}	45	
	ε_{33}	29	
Density(kg/m^3)	ρ	4850	
Coefficient of Thermal Enpension (ppm/K) [24]	α_x	14.4	
	α_y	15.9	
	α_z	7.5	

where a is the transformation matrix defined in terms of the Euler angles and M is the bond matrix. The material constants referred to a Z-cut oriented LN film are listed in Table II.

The obtained matrices are then input into the device model to calculate the resulting electromechanical coupling for $S0$-mode lamb wave. The specific simulation results are shown in Section V and directly compared to the relevant experimental data.

IV. DEVICE FABRICATION

Although LN material has drawn considerable attention in making electro-optical devices and RF microelectromechanical systems (RF-MEMS) resonators, it still remains a great challenge to attain a suspended LN thin film of bulk quality. This challenge is twofold for it encompasses first the integration of LN thin film on micromachinable substrates, and secondly the suspension of the thin film leveraging a number of micromachining techniques.

Several techniques from various research groups have been under development to enable a range of device based on LN material. Intuitively, it is desirable to integrate LN thin film on Si for the integration with semiconductor electronics. However, the lattice constant and coefficient of temperature expansion (CTE) mismatch between these two materials makes bonding extremely difficult. Several thin film deposition methods, including sputtering [25], [26], chemical vapor deposition (CVD) [27], and epitaxial growth [28], [29], have been attempted on various substrates. The film quality, as characterized by X-ray diffraction (XRD) rocking curve measurements, is still far from approaching bulk quality. Moreover, techniques of this nature are inherently limited to growing c axis (Z-cut) film. Z-cut LN is proven to have great optical properties [30], and preferred for electro-optical waveguide devices. However, RF-MEMS devices pursuing high electromechanical coupling are better served with Y- or X-cut LN thin film. Recently, more groups [16], [31] have successfully demonstrated transfer of thin film LN on either Si [32], [33] or LN [16] substrates using the crystal ion slicing technique. This technique uses two wafers, a donor wafer of LN, and a carrier wafer of LN or Si. The donor wafer is first implanted with high energy He+ or H+ ion beam, which is used to introduce micro cracks in the donor wafer. The implanted ion density and distribution inside the thin film is a function of the dose and energy of the implantation ions. The donor wafer is then bonded to the carrier wafer using either direct [16], [34] or adhesive bonding techniques [31]. The bonded wafers then go through heat treatment to make the preformed micro cracks expand and induce splitting [16]. This results in a thin transfer layer of donor material on a carrier substrate. An additional step of chemical mechanical polishing (CMP) may be carried out to fully remove the ion damaged portion of the transfer layer and subsequently obtain surface roughness less than 5-nm root mean square (rms). There are several challenges associated with this technique. First, the implantation energy and dose have to be properly chosen to facilitate the splitting in the subsequent fabrication step. The optimum energy and dose can be identified by a so-called blistering test. This test was previously used in Smart-Cut technology to identify the proper energy and dose for transferring bulk quality Si on oxide coated Si substrate. Additionally, the definition of the resonator boundaries requires anisotropic etch of the LN material. In the past, fluorine-based reactive ion etch (RIE) recipes have been developed for various cuts of LN with moderate etch rates [35]. These etch processes are highly physical and result in heavy re-deposition. The post etch surface is very rough and sidewalls are generally covered by LiF_2 byproducts. Moreover, the etch rate is low, ranging from 4 to 20 nm/min for various cuts of LN. The low etch rate, along with the re-deposition, makes it impractical to build high performance acoustic resonators with such recipe. In this work, a Cl_2-based RIE recipe is developed for the first time to etch different cuts of LN, and its parameters are listed in Table III. A Trion[1] etch system is used. The etch rates for various cuts are also listed in Table III, and resulting sidewall profiles are shown in Fig. 4. The etch rate varies for each cut and Y-cut is proven to be the most difficult to form smooth etched surface due to heavy re-deposition of the etch byproducts. The resulting sidewalls for X- and Z-cut are generally free of re-deposition and have sloped profiles. As it will be further discussed, the sidewall profiles can have an impact on the device k_t^2 and Q.

In this work, the fabrication process (Fig. 5) of LN microresonators starts with the ion implantation of the LN donor wafer. A proper dose is chosen to enable high yield splitting at low temperature ($< 350\ ^\circ$C). After the implantation, the donor LN

TABLE III
CHLORINE-BASED RIE RECIPE FOR LN MATERIAL

Parameter	Value
Cl_2 flow	5 sccm
BCl_3 flow	25 sccm
Ar flow	5 sccm
RIE power	250 W
ICP power	600 W
Chamber pressure	10 mTorr
Chamber Temperature	70 C°
Etch rate(X-cut)	45 nm/min
Etch rate(Y-cut)	80 nm/min
Etch rate(Z-cut)	100 nm/min

[1]Trion is a registered trademark of Trion Technology Inc., Clearwater, FL.

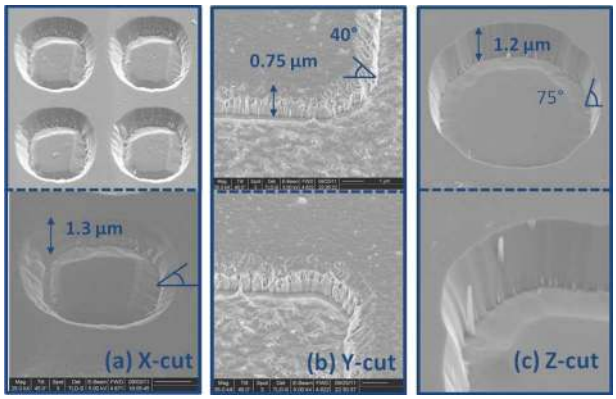

Fig. 4. SEM images of RIE etched sidewall profile for various cuts.

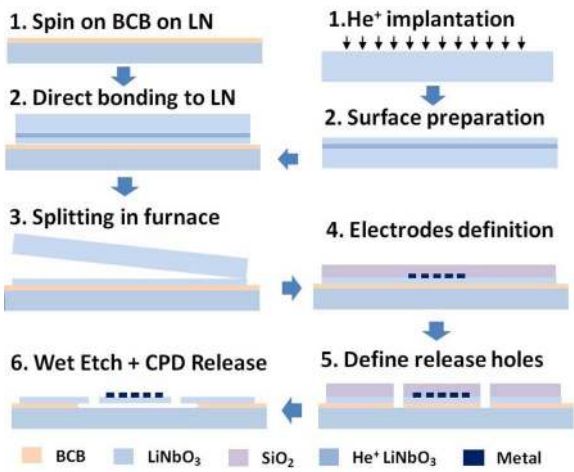

Fig. 5. Flowchart for the LN MEMS resonator fabrication process.

wafer is adhesively bonded to a LN carrier wafer with a thin layer of spin-on benzocyclobutene (BCB). This BCB layer serves as a sacrificial layer for releasing the micromechanical resonator. The sample then goes through heat treatments to carry out splitting. The ion slicing technique allows a thin film of bulk quality to be transferred on a carrier substrate for micromachining. The film transfer in this work is done by an external vendor, Srico Inc.[2] Inter-digital fingers (5-nm Ti/60 nm Al) are deposited on the LN thin film, followed by a Cl_2-based RIE step described before to define the boundaries for the resonant structure. Lastly, wet etch is used to remove the BCB layer under the resonant structure. Critical point drying (CPD) is performed to enable full suspension post BCB removal.

V. Experimental Results and Discussion

A. Device Admittance Response

Two groups of devices with orientations from 0° to 160° to the $+Y$ axis in the X-cut plane were fabricated on the same sample to verify the optimal orientation for high electromechanical coupling. The dimensions of the devices are listed in Table IV.

Two fabricated devices are shown in Fig. 6(a) and (b). These devices are measured at room temperature and in ambient air with a vector network analyzer and probe station. A short load open through (SLOT) calibration was performed to shift the measurement reference planes to the probe tips. As seen in Fig. 7, the finite-element analysis (FEA) performed with COMSOL exhibits excellent agreement with the measured results. The devices demonstrate a motional resistance as low as 120 Ω. Multiple resonances are excited and identified. For

[2]Srico is registered trademark of Srico Inc., Columbus, OH.

TABLE IV
LN Resonator Design Parameters

Parameter	W_p	W_f	N	W_g	t_{LN}	L_f
Design 1	6 μm	4 μm	8	3 μm	1 μm	120μm
Design 2	6 μm	4 μm	16	3 μm	1 μm	120μm

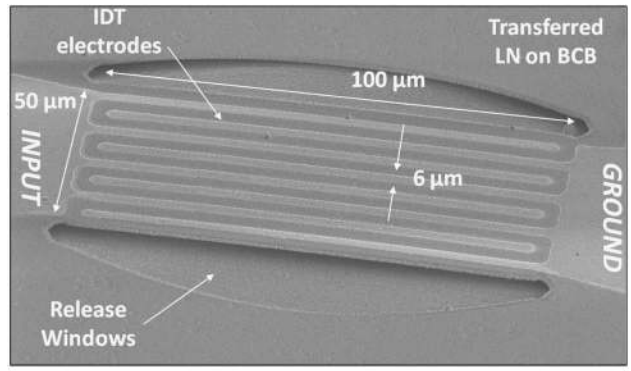

(a) Design 1

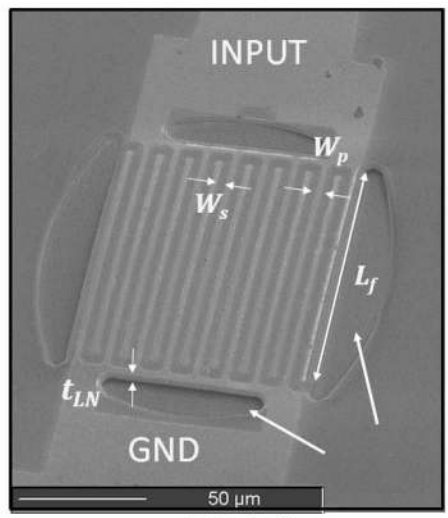

(b) Design 2

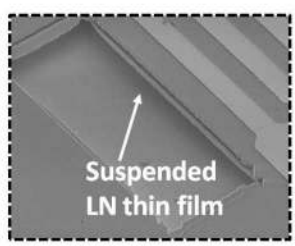

(c) Suspended LN thin film edge

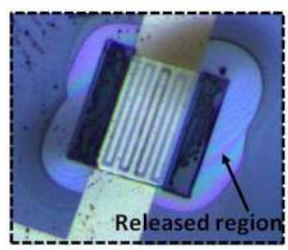

(d) Optical Image of a released device (design 1)

Fig. 6. (a) and (b) SEM images of fabricated resonators (design 1 and 2) with the dimensions listed in Table IV. (c) Zoomed-in view of the suspended LN thin film and its sidewall. (d) Isotropic etch of BCB for device release. (a) Design 1. (b) Design 2. (c) Suspended LN thin film edge. (d) Optical image of a released device (design 1).

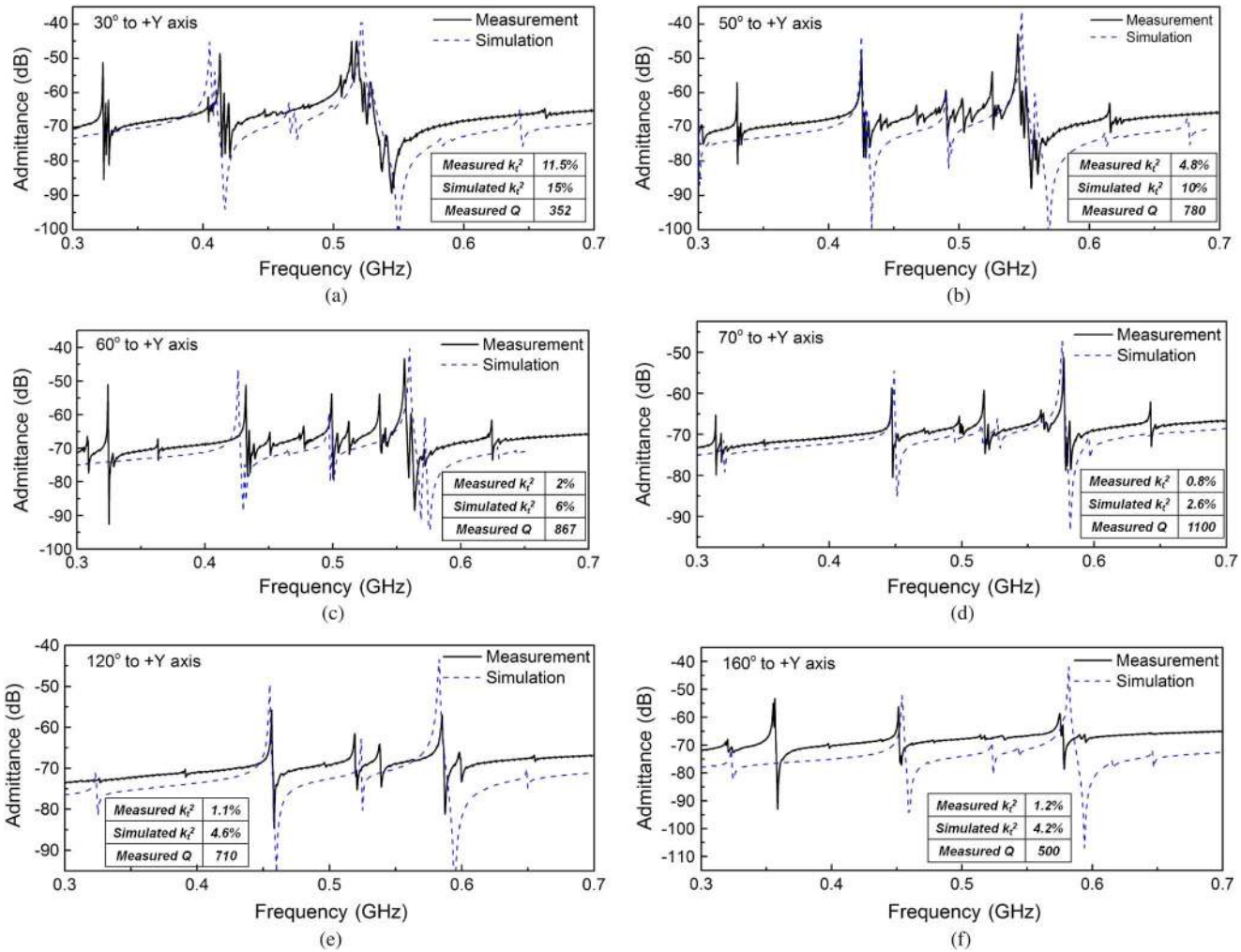

Fig. 7. Measured and simulated admittance response of fabricated LFE LN resonators with various orientations. (a) 30°. (b) 50°. (c) 60°. (d) 70°. (e) 120°. (f) 160°.

example (Fig. 8), the device with an orientation of 40° to $+Y$ axis shows two pronounced $S0$-mode resonances centered at 410 MHz [see Fig. 8(b)] and 520 MHz [see Fig. 8(c)]. The displacement mode shapes confirm that the vibrations are indeed $S0$ mode. The spacing of the $S0$ mode overtone resonances is set by the overall width $(N \cdot W_f)$ of the resonator, similarly to previously demonstrated LOBAR devices [36]. The excitation of multiple overtones is expected with devices using high piezoelectric coupling materials such as LN. However, it is not desired because it can subdue the energy coupling into the intended fundamental $S0$ mode, and therefore reduce the achievable k_t^2. Several techniques are currently under development to predominantly excite only one of the overtones at the desired center frequency. Several unwanted spurious modes are also observed in the spectral vicinity of the $S0$ mode overtones. This is also commonly noted for lamb wave device. These modes are identified as asymmetric modes (A0 like), as shown in Fig. 8. Such asymmetric modes can be suppressed with optimized electrode patterns [37] and will be further investigated for LN resonator as well. The device has also shown subdued HBAR-type vibrations excited at the probe pads location. The 5-MHz spacing between adjacent resonances correspond to the 500-μm LN substrate.

The experimental results are also summarized in Table V for both designs covering all orientation. The fabrication yield remains modest due to built-in stress gradient in the LN thin film. Some of the released devices failed post release due to stress induced cracking at the anchors.

B. Electromechanical Coupling (k_t^2) and C_0

The measured k_t^2, as shown in Fig. 9, displays a lower value than the simulated results. This is because the feed-through capacitance (C_f) is not considered in the FEM model. To experimentally characterize the feed through capacitance induced by the probe pads, dummy structures shown in Fig. 10(a) were also fabricated on the same die with different orientations. The feed through testing structures have the same dimensions as the resonator devices, except that the IDTs are removed. The static capacitance and feed-through capacitance are both extracted from the admittance measurements and plotted in Fig. 10(b) with simulated C_0 values also displayed. The difference between the measured static capacitance $(C_0 + C_f)$ and simulated C_0 can

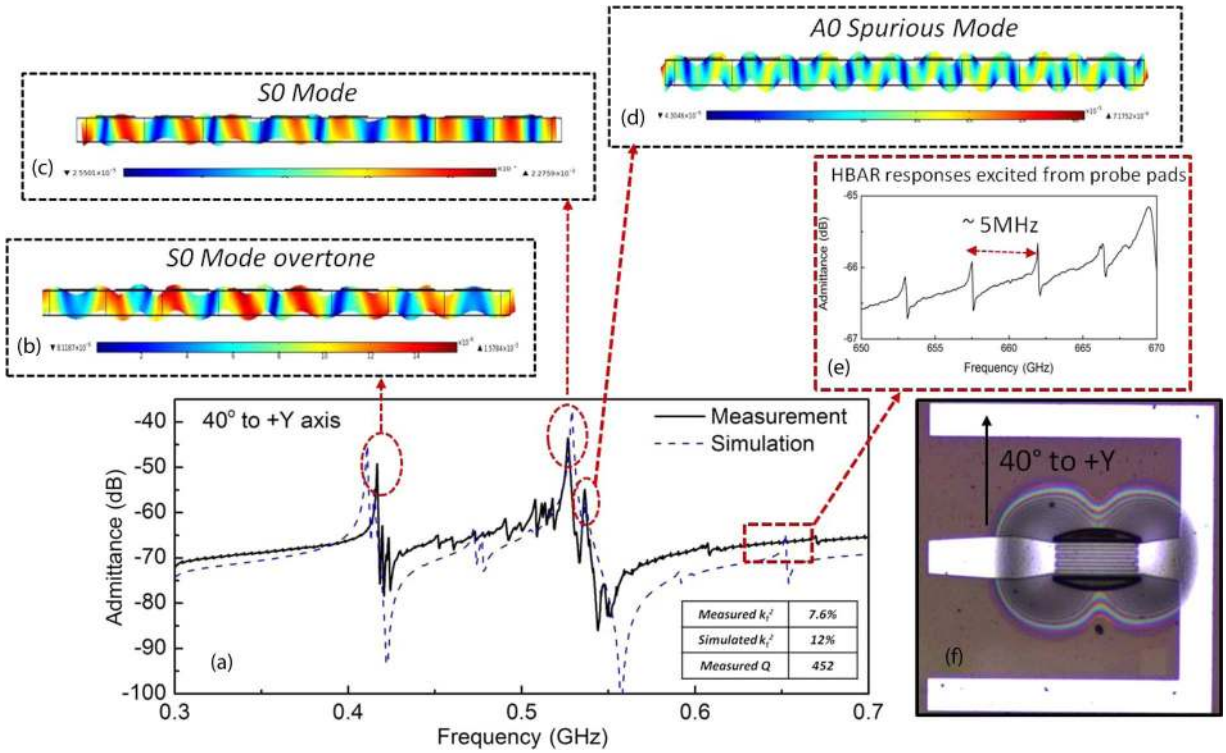

Fig. 8. (a) Measured and simulated admittance response of the LN resonator with an orientation of 40° to $+Y$ axis, with displacement mode shapes for each resonance (b)–(d) highlighted. The zoomed-in view of the HBAR response excited by GSG probe pads is shown in (e), and the optical microscope image of the measured device is shown in (f).

be readily accounted for given the measured C_f. The high C_f value (around 60 fF) is due to the high dielectric constants of LN (see Table II), and can be used to explain the mismatch between the measured and simulated k_t^2. Since C_f is determined by the testing layout, ground–signal–ground (GSG) probe pads with larger separation can be used to minimize the feed-through capacitance. Larger resonators with a higher C_0 are also expected to exhibit a lower impact of C_f on k_t^2.

C. Quality Factor (Q)

Theoretically, the Q is influenced by a number of damping mechanisms [38] and its enhancement remains an active research topic in the acoustic resonator community. The loss mechanisms for MEMS resonators and their impact on device performance are still under investigation [39]–[41]. Although it is hard to pinpoint the sources of loss in the thin film LN devices of this work, it is believed that the currently demonstrated quality factors are far from the ultimate limit set by the phonon–phonon dissipation in the piezoelectric material. LN material is theoretically predicted [38] and experimentally verified to have very low intrinsic acoustic loss [6]. The $f \cdot Q$ limit for LN is as high as 5×10^{13}, far exceeding other piezoelectric materials (AlN, ZnO, and PZT) and silicon. However, this figure is for bulk LN and the transferred thin film LN Q has never been extracted and reported. Researchers have investigated the distribution of implantation induced defects in thin film LN along with methods of defect mitigation [42]. The distribution of defects is critical to achieve high Q operation since it can scatter the acoustic wave and degrade the material Q. It has been shown that with post-implantation low temperature annealing ($< 350\,^{\circ}\mathrm{C}$) and polishing, the damage and defects can be either mitigated or removed, restoring the original high quality of the bulk material. Further investigations on the impact of annealing on the device Q need to be performed in order to understand the impact of this loss mechanism on the thin film LN resonators of this work. Other loss mechanisms are related to the metallization layer, especially intrinsic material and interface losses. The devices demonstrated in this work use aluminum as the electrode material due to its low acoustic and interface losses [43] and high conductivity. The devices shown in this work have a 300% enhancement in Q compared to previous work from the same authors with Au electrodes [13].

The quality factors of these devices have also shown a dependence on the device orientation. This is likely caused by the orientation dependent sidewall definition (Fig. 11) in the developed RIE recipe (Table III). The SEM images of the acoustic boundaries defined by RIE are shown in Figs. 4(a) and 6(c). It is clear that a higher sloped sidewall is present at angles for which low Q's are also observed. The sloped sidewall is known to have a detrimental effect on laterally vibrating resonator since the sidewall serves as the acoustic wave reflector and nonstraight profile can induce unwanted acoustic wave scattering. The slope can also introduce unintended flexural modes and degrade the k_t^2 of the desired mode [4]. The orientation-dependent sidewall definition in RIE is most likely due to the anisotropy of the LN material. The quality factor of the devices with high electromechanical coupling orientations are expected to improve significantly once the RIE is further optimized to yield a straight sidewall profile. The fabricated freestanding thin films also display warping

TABLE V
EXPERIMENTAL RESULTS SUMMARY FOR THE FABRICATED RESONATORS ON THE SAME SAMPLE IN TERMS OF RESONANT FREQUENCY (f_0), ELECTROMECHANICAL COUPLING (k_t^2), QUALITY FACTOR (Q), AND MOTIONAL RESISTANCE (R_m)

Orientation to +Y axis	Design 1 f_0(MHz)	Design 1 k_t^2(%)	Design 1 Q	Design 1 $R_m(\Omega)$	Design 2 f_0(MHz)	Design 2 k_t^2(%)	Design 2 Q	Design 2 $R_m(\Omega)$
0°	-	-	-	-	553	2.3	424	181
10°	-	-	-	-	558	0.99	593	794
20°	526.4	9.65	152	447	560.1	3	655	760
30°	517.8	11.5	358	178	566.2	2.8	845	810
40°	526.7	7.6	452	146	-	-	-	-
50°	545.1	4.8	780	108	516.8	0.55	1270	562
60°	567.3	2	867	112	527.4	1.2	1780	110
70°	577	0.8	1100	355	527.4	1.2	1780	110
80°	590.4	0.8	130	1580	-	-	-	-
90°	-	-	-	-	582	0.99	1869	112
100°	-	-	468	-	582.3	0.88	1176	206
110°	575	0.72	678	668	578.5	0.89	853	479
120°	585.1	1.12	550	709	572	1.15	1380	207
130°	570.2	0.99	693	470	568.3	0.99	553	733
140°	575	0.99	422	794	-	-	-	-
160°	581	1.2	500	820	-	-	-	-

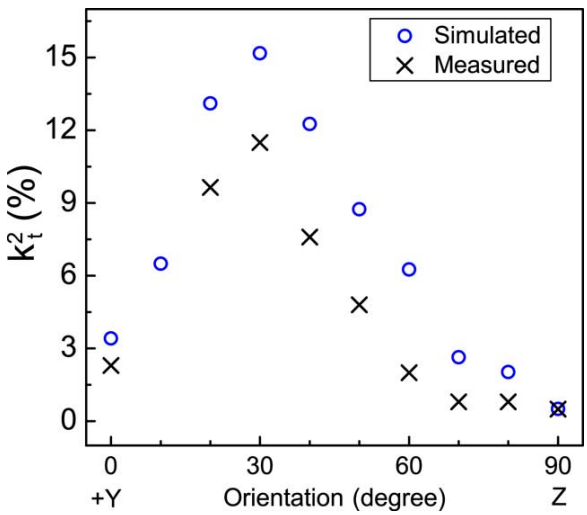

Fig. 9. Comparison between measured and simulated k_t^2 for LN resonators with various orientations.

and bowing. Acoustic energy could leak into the carrier substrate, and subsequently reduce Q if any contact between the released thin film and carrier substrate is present. In order to prevent the post-release thin film from contacting the carrier, the anchoring mechanisms of these demonstrated devices (shown in Fig. 6) are either based on fully tethered (design 1) or four corner suspension (design 2) type of configurations. Nevertheless, the released devices still exhibit an upward curvature due to stress gradient built up in the fabrication process. It is believed that this can have a number of effects on the device performance, such as shifting the phase velocity by stress induced stiffening and degradation of Q due to curvature induced acoustic wave scattering. The large size anchors that were used could also be introducing additional energy loss to the device surroundings. It is believed that the device Q is still far from the ultimate value possible with LN thin films and it is currently limited by the fabrication process. The film stress gradient is currently being experimentally studied, and better understanding and control of the stress is expected to improve the device yield and enhance the Q simultaneously.

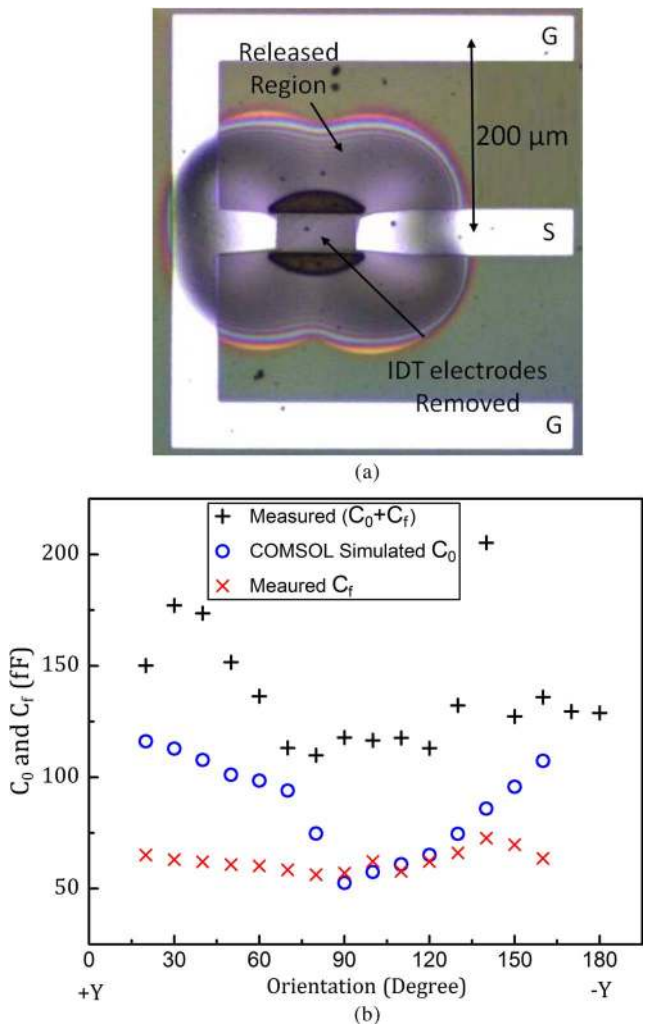

Fig. 10. (a) Optical image of feed-though testing structure and (b) measured static capacitance, simulated C_0 values and feed-through (C_f) of the resonator versus orientations.

D. Temperature Stability

The TCF for LN resonators with various orientations was also measured. The measurements were performed with a TTP-6

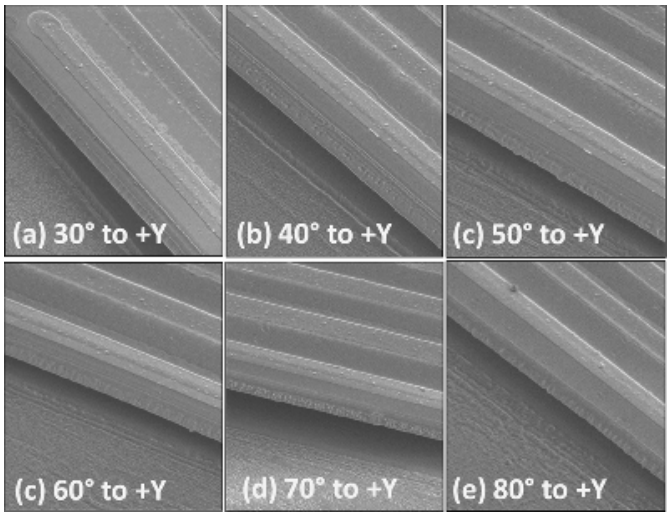

Fig. 11. Dependence of sidewall RIE definition on device orientation.

Lakeshore[3] probe station and network analyzer. The devices were cycled multiple times between 300–400 K with a step of 10 K, and admittance measurements were taken 5 min after the target temperature was reached. Devices with orientations of 0°, 30°, 50°, 70°, and 90° to $+Y$ axis were tested. The measured TCFs are shown in Fig. 12. The device with a 30° orientation shows the highest TCF of -67.8 ppm/K, while the device with 70° orientation shows the lowest TCF of -55.4 ppm/K.

The TCF of Lamb wave resonators can be analyzed with the following simplified equation [4]:

$$\mathrm{TCF} = -\alpha_1 + \frac{1}{2}(2\alpha_1 + \alpha_3) + \frac{1}{2}\frac{\partial \ln E_p}{\partial T} \tag{10}$$

where α_1 and α_3 are the linear coefficient of thermal expansion in the plane and out-of-plane directions, respectively. Hence, for X-cut, α_3 is in the direction of the X axis and α_1 is aligned with the propagation direction of the acoustic wave. Thus, in the case of X-cut, the TCF can be approximately formulated as

$$\mathrm{TCF} = -\alpha_\theta + \frac{1}{2}\alpha_x + \frac{1}{2}\frac{\partial c_\theta}{\partial T} \tag{11}$$

where α_θ and α_x are the coefficient of thermal expansion along the orientation of the device within the Y–Z plane and X axis, respectively. α_θ can be calculated using tensor rotation [see (7)] and the values used are listed in Table II. $\partial c_\theta/\partial T$ is the TCF for the stiffness constant along the direction of acoustic-wave propagation, which can be extracted by tensor rotation and previously reported TCF values for the stiffness matrix (Table II). The calculated TCF versus device orientation is illustrated in Fig. 13 with the measured values. The measurements exhibit a good agreement with the theoretical predictions. The slight mismatch between measured and calculated TCF for the device oriented 70° to $+Y$ axis is most likely caused by the observed high tensile stress in this orientation. It has been shown that tensile stress can decrease the TCFs for double-clamped micromechanical resonators [44]. The TCF of laterally vibrating MEMS resonators is lower than temperature uncompensated LN SAW devices (85–110 ppm/K) [45]. Such TCF translates to a 0.65% shift for a temperature range of 100 K. This is tolerable for wideband filtering, as most standards (GSM, CDMA, and ISM) have a 3% or lager gap between transmitting and receiving bands.

[3]Lakeshore is registered trademark of Lake Shore Cryotronics Inc., Westerville, OH.

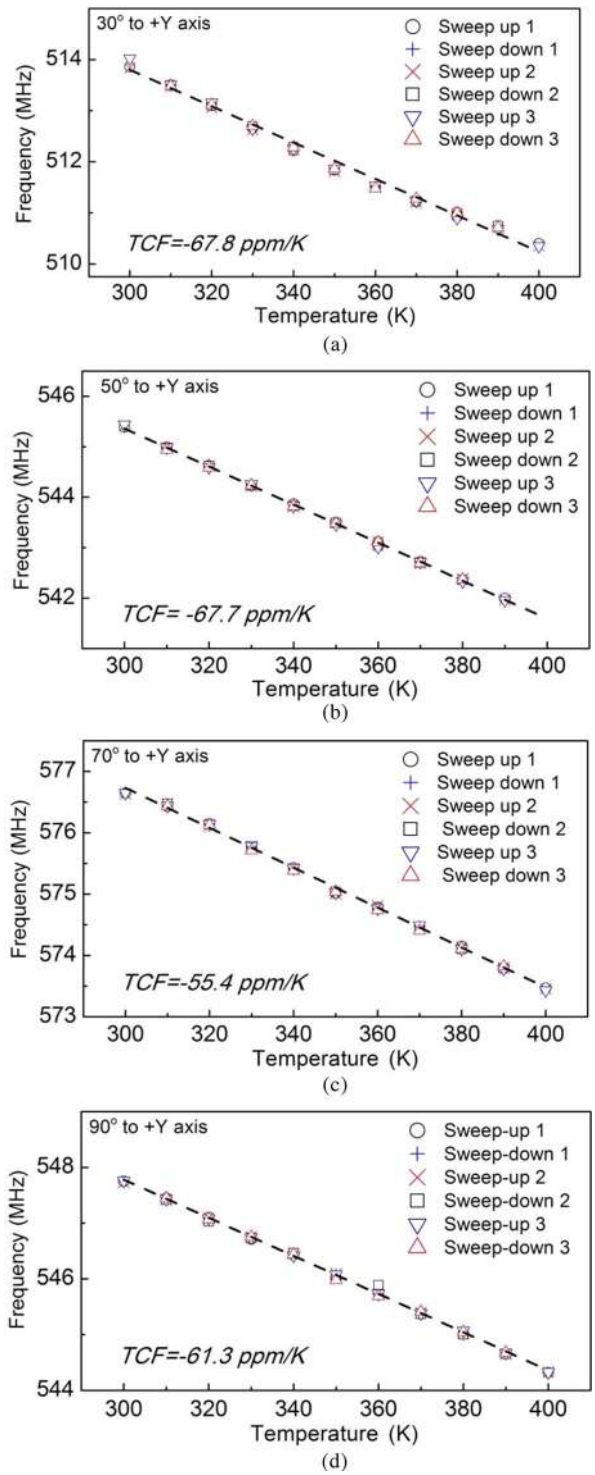

Fig. 12. Measured TCF of LN resonators with various orientations. (a) TCF measurement for the device oriented 30° to $+Y$ axis. (b) TCF measurement for the device oriented 50° to $+Y$ axis. (c) TCF measurement for the device oriented 70° to $+Y$ axis. (d) TCF measurement for the device oriented 90° to $+Y$ axis.

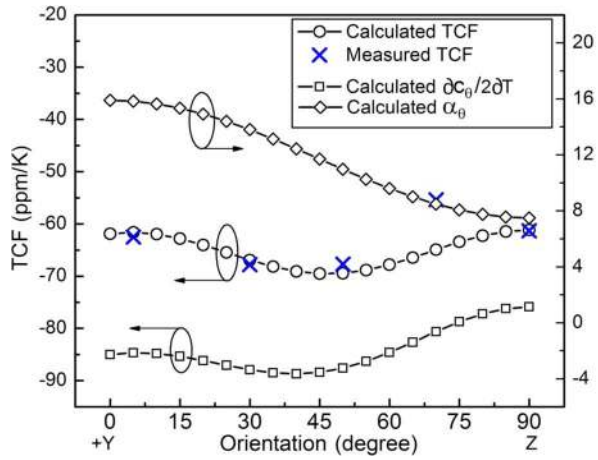

Fig. 13. Comparison between the measured and calculated TCF [see (11)] versus device orientation.

TABLE VI
MEASURED BIFURCATION POINTS FOR LN MEMS RESONATORS

Orientation (to +Y axis)	Bifurcation Power (dBm)
0°	2.8
30°	3.4
50°	2.9
70°	2.5
90°	2.7

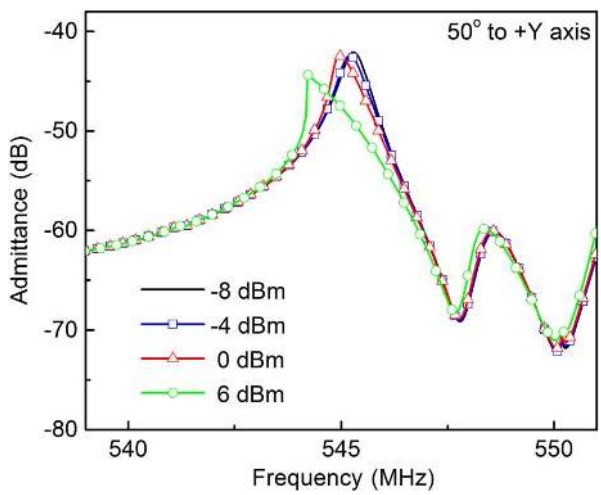

Fig. 14. Example power-handling measurements on LN resonator with an orientation of 50° to $+Y$ axis. The output power of the network analyzer is listed in the legend at various levels.

E. Power Handling and Nonlinearity

The nonlinear behavior and power-handling capability of the LN microresonators were experimentally investigated by measuring the admittance response at various power input levels to identify the device bifurcation point. For MEMS resonators, the bifurcation is defined as the input power at which magnitude or phase shows a vertical slope in an amplitude-frequency sweep and displays the verge of instability. This corresponding level of input power can be considered as the highest level of power that the device can handle before large nonlinearity is recorded. The input power was swept from -10 to $+10$ dBm for devices oriented at 0°, 30°, 50°, 70°, and 90° to $+Y$ axis. Their corresponding bifurcation power levels are listed in Table VI. The power listed has been adjusted to take account the reflections caused by the non-50-Ω impedance of each resonator. An example power sweep measurement is shown in Fig. 14 for the device oriented at 50° to $+Y$ axis. The resonance peak bends as the input power increases. At 6 dBm, the response exhibits the verge of instability. The tested LN resonators display similar nonlinearity and power handling capabilities as AlN $S0$-mode resonators [46].

VI. CONCLUSION

The first laterally vibrating microresonators using ion sliced X-cut LN thin film were designed and fabricated. This new type of devices is enabled by a novel fabrication process involving ion slicing, adhesive bonding, and selective etching and releasing. The design of such devices, including its orientation within the X-cut LN plane and electrode configuration were analyzed with the FEM using COMSOL. The results indicate that the k_t^2 is a function of the device orientation and maximum when the device is positioned between 30°–40° to $+Y$ axis. Multiple prototype devices ($f_c = 500$ MHz), with an orientation spanning from 0° to 160° to $+Y$ axis, were fabricated and tested. The device oriented 30° to $+Y$ has a k_t^2 of 11.5%, the highest among any demonstrated laterally vibrating MEMS resonators to date. This first prototype holds strong potential for enabling a new wide bandwidth and reconfigurable RF filtering platform. Detailed characterization on device Q, static capacitance C_0, TCF, and power handling is also presented and analyzed. Future work will focus on enhancing the resonator Q by optimizing the fabrication process, controlling the residual stress, redefining the structural suspensions, and optimizing electrode design to suppress unwanted modes of vibration.

REFERENCES

[1] R. Ruby, P. Bradley, I. Larson, J. , Y. Oshmyansky, and D. Figueredo, "Ultra-miniature high-Q filters and duplexers using FBAR technology," in *IEEE Int. Solid-State Circuits Conf. Tech. Dig.*, 2001, pp. 120–121, 438.

[2] Q.-X. Su, P. Kirby, E. Komuro, M. Imura, Q. Zhang, and R. Whatmore, "Thin-film bulk acoustic resonators and filters using ZnO and leadzirconium-titanate thin films," *IEEE Trans. Microw. Theory Techn.*, vol. 49, no. 4, pp. 769–778, Apr. 2001.

[3] C. D. Corso, A. Dickherber, and W. D. Hunt, "Lateral field excitation of thickness shear mode waves in a thin film ZnO solidly mounted resonator," *J. Appl. Phys.*, vol. 101, no. 5, pp. 054 514–054 514-7, Mar. 2007.

[4] G. Piazza, P. Stephanou, and A. Pisano, "Piezoelectric aluminum nitride vibrating contour-mode MEMS resonators," *J. Microelectromech. Syst.*, vol. 15, no. 6, pp. 1406–1418, Dec. 2006.

[5] A. Reinhardt, E. Defay, F. Perruchot, and C. Billard, "Tunable composite piezoelectric resonators: A possible Holy Grail of RF filters," in *IEEE MTT-S Int. Microw. Symp. Dig.*, Jun. 2012, pp. 1–3.

[6] M. Pijolat, A. Reinhardt, E. Defay, C. Deguet, D. Mercier, M. Aid, J. Moulet, B. Ghyselen, D. Gachon, and S. Ballandras, "Large Qxf product for HBAR using smart cut transfer of LiNbO3 thin layers onto LiNbO3 substrate," in *IEEE Ultrason. Symp.*, Nov. 2008, pp. 201–204.

[7] C. Zuo, J. Van Der Spiegel, and G. Piazza, "1.05-GHz CMOS oscillator based on lateral-field-excited piezoelectric AlN contour-mode MEMS resonators," *IEEE Trans. Ultrason., Ferroelect., Freq. Control*, vol. 57, no. 1, pp. 82–87, Jan. 2010.

[8] X. Zhu, J. Phillips, and A. Mortazawi, "A DC voltage dependant switchable thin film bulk wave acoustic resonator using ferroelectric thin film," in *IEEE MTT-S Int. Microw. Symp. Dig.*, Jun. 2007, pp. 671–674.

[9] M. Rinaldi, C. Zuniga, C. Zuo, and G. Piazza, "Super-high-frequency two-port AlN contour-mode resonators for RF applications," *IEEE Trans. Ultrason., Ferroelectr., Freq. Control*, vol. 57, no. 1, pp. 38–45, Jan. 2010.

[10] T. Kimura, M. Kadota, and Y. Ida, "High Q SAW resonator using upperelectrodes on grooved-electrodes in LiTaO3," in *IEEE MTT-S Int. Microw. Symp. Dig.*, May 2010, pp. 1740–1743.

[11] M. Pijolat, S. Loubriat, S. Queste, D. Mercier, A. Reinhardt, E. Defay, C. Deguet, L. Clavelier, H. Moriceau, M. Aid, and S. Ballandras, "Large electromechanical coupling factor film bulk acoustic resonator with X-cut LiNbO3 layer transfer," *Appl. Phys. Lett.*, vol. 95, no. 18, pp. 182 106–182 106-3, Nov. 2009.

[12] Y.-W. Lin, S.-S. Li, Z. Ren, and C. Nguyen, "Low phase noise array-composite micromechanical wine-glass disk oscillator," in *IEEE Int. Electron Devices Meeting Tech. Dig.*, Dec. 2005, pp. 4, 281.

[13] S. Gong, L. Shi, and G. Piazza, "High electromechanical coupling MEMS resonators at 530 MHz using ion sliced X-cut LiNbO3 thin film," in *IEEE MTT-S Int. Microw. Symp. Dig.*, Jun. 2012, vol. 1, pp. 1–5.

[14] J.-H. Lee, I. Bargatin, J. Provine, F. Liu, M.-K. Seo, R. Maboudian, M. Brongersma, N. Melosh, Z. Shen, and R. Howe, "Effect of illlumination on thermionic emission from microfabricated silicon carbide structures," in *16th Int. Solid-State Sens., Actuators, Microsyst. Conf.*, Jun. 2011, pp. 2658–2661.

[15] N.-K. Kuo, S. Gong, J. Hartman, J. Kelliher, W. Miller, J. Parke, S. Krishaswamy, J. Adam, and G. Piazza, "Micromachined sapphire GHz lateral overtone bulk acoustic resonators transduced by aluminum nitride," in *IEEE 25th Int. MEMS Conf.*, Feb. 2012, pp. 27–30.

[16] M. Levy, R. M. Osgood, R. Liu, L. E. Cross, G. S. Cargill, A. Kumar, and H. Bakhru, "Fabrication of single-crystal lithium niobate films by crystal ion slicing," *Appl. Phys. Lett.*, vol. 73, no. 16, pp. 2293–2295, Oct. 1998.

[17] R. Abdolvand, H. Lavasani, G. Ho, and F. Ayazi, "Thin-film piezoelectric-on-silicon resonators for high-frequency reference oscillator applications," *IEEE Trans. Ultrason., Ferroelect., Freq. Control*, vol. 55, no. 12, pp. 2596–2606, Dec. 2008.

[18] H. Chandrahalim, S. A. Bhave, R. Polcawich, J. Pulskamp, D. Judy, R. Kaul, and M. Dubey, "Performance comparison of pb(zr0.52ti0.48)o3-only and pb(zr0.52ti0.48)o3-on-silicon resonators," *Appl. Phys. Lett.*, vol. 93, no. 23, pp. 233 504–233 504-3, Dec. 2008.

[19] I. Kuznetsova, B. Zaitsev, S. Joshi, and I. Borodina, "Investigation of acoustic waves in thin plates of lithium niobate and lithium tantalate," *IEEE Trans. Ultrason., Ferroelect., Freq. Control*, vol. 48, no. 1, pp. 322–328, Jan. 2001.

[20] S. Gevorgian, T. Martinsson, P. Linner, and E. Kollberg, "CAD models for multilayered substrate interdigital capacitors," *IEEE Trans. Microw. Theory Techn.*, vol. 44, no. 6, pp. 896–904, Jun. 1996.

[21] B. A. Auld, *Acoustic Fields and Waves in Solids*. Melbourne, FL: Krieger, 1990.

[22] G. Kovacs, M. Anhorn, H. Engan, G. Visintini, and C. Ruppel, "Improved material constants for LiNbO3 and LiTaO3," in *Proc. IEEE Ultrason. Symp.*, Dec. 1990, vol. 1, pp. 435–438.

[23] R. T. Smith and F. S. Welsh, "Temperature dependence of the elastic, piezoelectric, and dielectric constants of lithium tantalate and lithium niobate," *J. Appl. Phys.*, vol. 42, no. 6, pp. 2219–2230, May 1971.

[24] H. Ogi, Y. Kawasaki, M. Hirao, and H. Ledbetter, "Acoustic spectroscopy of lithium niobate: Elastic and piezoelectric coefficients," *J. Appl. Phys.*, vol. 92, no. 5, pp. 2451–2456, Sep. 2002.

[25] H. Akazawa and M. Shimada, "Correlation between interfacial structure and c-axis-orientation of LiNbO3 films grown on Si and SiO2 by electron cyclotron resonance plasma sputtering," *J. Crys. Growth*, vol. 270, no. 3, pp. 560–567, 2004.

[26] S. Tan, T. Gilbert, C. A. Hung, T. E. Schlesinger, and M. Migliuolo, "Sputter deposited c-oriented LiNbO3 thin films on SiO2," *J. Appl. Phys.*, vol. 79, no. 7, pp. 3548–3553, Apr. 1996.

[27] M. Kadota, T. Ogami, K. Yamamoto, H. Tochishita, and Y. Negoro, "High-frequency lamb wave device composed of MEMS structure using LiNbO3 thin film and air gap," *IEEE Trans. Ultrason., Ferroelect., Freq. Control*, vol. 57, no. 11, pp. 2564–2571, Nov. 2010.

[28] D. Saulys, V. Joshkin, M. Khoudiakov, T. Kuech, A. Ellis, S. Oktyabrsky, and L. McCaughan, "An examination of the surface decomposition chemistry of lithium niobate precursors under high vacuum conditions," *J. Crys. Growth*, vol. 217, no. 3, pp. 287–301, 2000.

[29] R. Betts and C. Pitt, "Growth of thin-film lithium niobate by molecular beam epitaxy," *Electron. Lett.*, vol. 21, no. 21, pp. 960–962, 1985, 10.

[30] L. Arizmendi, "Photonic applications of lithium niobate crystals," *Phys. Status Solidi (a)*, vol. 201, no. 2, pp. 253–283, 2004.

[31] G. Poberaj, M. Koechlin, F. Sulser, A. Guarino, J. Hajfler, and P. Gunter, "Ion-sliced lithium niobate thin films for active photonic devices," *Opt. Mater.*, vol. 31, no. 7, pp. 1054–1058, 2009.

[32] K. Diest, M. J. Archer, J. A. Dionne, Y.-B. Park, M. J. Czubakowski, and H. A. Atwater, "Silver diffusion bonding and layer transfer of lithium niobate to silicon," *Appl. Phys. Lett.*, vol. 93, no. 9, pp. 092 906–092 906-3, Sep. 2008.

[33] M. Solal, T. Pastureaud, S. Ballandras, B. Aspar, B. Biasse, W. Daniau, J. Hode, S. Calisti, and V. Laude, "Oriented lithium niobate layers transferred on 4 $''$ [100] silicon wafer for RF SAW devices," in *Proc. IEEE Ultrason. Symp.*, Oct. 2002, vol. 1, pp. 131–134.

[34] P. Rabiei and W. H. Steier, "Lithium niobate ridge waveguides and modulators fabricated using smart guide," *Appl. Phys. Lett.*, vol. 86, no. 16, pp. 161 115–161 115-3, Apr. 2005.

[35] S. Benchabane, L. Robert, J.-Y. Rauch, A. Khelif, and V. Laude, "Highly selective electroplated nickel mask for lithium niobate dry etching," *J. Appl. Phys.*, vol. 105, no. 9, pp. 094 109–094 109-6, May 2009.

[36] S. Gong, N.-K. Kuo, and G. Piazza, "GHz high-Q lateral overmoded bulk acoustic-wave resonators using epitaxial SiC thin film," *J. Microelectromech. Syst.*, vol. 21, no. 2, pp. 253–255, Apr. 2012.

[37] M. Giovannini, S. Yazici, N.-K. Kuo, and G. Piazza, "Spurious mode suppression via apodization for 1 GHz AlN contour-mode resonators," in *IEEE Int. Freq. Control Symp.*, May 2012, pp. 1–5.

[38] S. Chandorkar, M. Agarwal, R. Melamud, R. Candler, K. Goodson, and T. Kenny, "Limits of quality factor in bulk-mode micromechanical resonators," in *IEEE 21st Int. MEMS Conf.*, Jan. 2008, pp. 74–77.

[39] L. Sorenson, J. Fu, and F. Ayazi, "One-dimensional linear acoustic bandgap structures for performance enhancement of AlN-on-silicon micromechanical resonators," in *16th In. Solid-State Sens., Actuators, Microsyst. Conf.*, Jun. 2011, pp. 918–921.

[40] L.-W. Hung and C.-C. Nguyen, "Capacitive-piezoelectric AlN resonators with Q 12,000," in *IEEE 24th Int. MEMS Conf.*, Jan. 2011, pp. 173–176.

[41] W. Wang and D. Weinstein, "Acoustic bragg reflectors for Qenhancement of unreleased MEMS resonators," in *Joint IEEE Int. Freq. Control Conf./Eur. Freq. and Time Forum*, May 2011, pp. 1–6.

[42] T. Gischkat, F. Schrempel, T. Hche, and W. Wesch, "Annealing behavior of lithium niobate irradiated with He-ions at 100 k," *Nucl. Instrum. Methods Phys. Res. B*, vol. 267, no. 8, pp. 1492–1495, 2009.

[43] M. Rinaldi, A. Tazzoli, J. Segovia-Fernandez, V. Felmetsger, and G. Piazza, "High power and low temperature coefficient of frequency oscillator based on a fully anchored and oxide compensated AlN contour-mode MEMS resonator," in *IEEE 25th Int. MEMS Conf.*, Feb. 2012, pp. 696–699.

[44] R. Melamud, M. Hopcroft, C. Jha, B. Kim, S. Chandorkar, R. Candler, and T. Kenny, "Effects of stress on the temperature coefficient of frequency in double clamped resonators," in *13th Int. Solid-State Sens., Actuators, Microsystems Tech. Dig.*, Jun. 2005, vol. 1, pp. 392–395.

[45] M. Patel, K. Bhattacharjee, J. Reed, and S. Zhgoon, "Temperature compensation of longitudinal leaky SAW with silicon dioxide overlay," in *IEEE Ultrason. Symp.* , Nov. 2008, pp. 1006–1010.

[46] J. Segovia-Fernandez, A. Tazzoli, M. Rinaldi, and G. Piazza, "Nonlinear lumped electrical model for contour mode AlN resonators," in *IEEE Int. Ultrason. Symp.*, Oct. 2011, pp. 1846–1849.

Songbin Gong (S'06–A'09) received the B.S. degree in electrical engineering from the Huazhong University of Science and Technology, Wuhan, China, in 2004, and the Ph.D. degree in electrical engineering from the University of Virginia, Charlottesville, in 2010.

From 2010 to 2012, he was a Postdoctoral Researcher with the Department of Electrical and Systems Engineering, University of Pennsylvania, Philadelphia. He is currently a Research Scientist with the Department of Electrical and Computer Engineering, Carnegie Mellon University, Pittsburgh, PA. He possesses over eight years of research experience on various RF MEMS devices. He has authored over 20 peer-reviewed publications. His research interests primarily include design and development of RF-MEMS devices, components, and subsystems for future RF front-ends.

Gianluca Piazza (S'00–M'06) received the Ph.D. degree from the University of California at Berkeley, in 2005.

He is currently an Associate Professor with the Department of Electrical and Computer Engineering, Carnegie Mellon University (CMU), Pittsburgh, PA. Prior to joining CMU, he was the Wilf Family Term Assistant Professor with the Department of Electrical and Systems Engineering (ESE), University of Pennsylvania. His research interests focus on piezoelectric microelectromechanical sytems and nanoelectromechanical systems (MEMS/NEMS) for RF wireless communication, chemical/biological detection, and all mechanical computing. He also has a general interest in the areas of microfabrication/nanofabrication techniques and integration of microdevices/nanodevices with state-of-the-art electronics. He possesses more than ten years of experience working with piezoelectric materials and devices. He holds several patents in the field of micromechanical resonators, some of which have been successfully acquired by industry.

Dr. Piazza was the recipient of the IBM Young Faculty Award in 2006. Along with his students, he has been the recipient of the Best Paper Award in Group 1 and 2 of the IEEE Frequency Control Symposium in 2008, 2009, and 2011.